Simulation of dredged sediment releases into homogeneous water using a two-phase model

Duc Hau Nguyen [a,b], Florence Levy [a,*], Damien Pham Van Bang [a], Sylvain Guillou [b], Kim Dan Nguyen [a], Julien Chauchat [c]

[a] Laboratory for Hydraulics Saint-Venant, Université Paris-Est, Joint-Research Unit, EDF/R&D-CETMEF-ENPC, 6 quai Watier, BP 49, 78401 Chatou Cedex, France
[b] Laboratoire Universitaire des Sciences Appliquées de Cherbourg (EA4253), Université de Caen, Site Universitaire de Cherbourg, BP 78, 50130 Cherbourg-Octeville, France
[c] Laboratoire d'Ecoulements Géophysiques et Industriels, CNRS UMR 5519, Université de Grenoble, BP 53, 38041 Grenoble Cedex 9, France

ARTICLE INFO

ABSTRACT

Dredging operations of navigation channels and harbours are regularly planned in order to maintain the nautical depth and to ensure the navigation safety. Depending on the quality of the dredged material (fixed by the Oslo convention, 1972), dredged sediments can be released into the sea or stored at the Earth's surface to be cleaned up. The present study deals with release operations. We simulate the complete process (generation and settling of a sediment plume, propagation of a density current on the bottom) using a two-phase flow model. We show that in this case, the sediment (or solid) phase strongly differs from the motion of the water (or fluid) phase. Comparisons between numerical results and experiments are carried out in order to illustrate the effects of sediment diameter, initial concentration, and ambient current on the plume dynamics and on the density current. We obtain a correct agreement with experiments for the specific release case.

1. Introduction

Yearly, a huge quantity of sediments is removed by dredging operations from inland waterways and navigation channels in estuarine zones. As land areas for storing dredged sediments are expensive, sediment release into the sea water is very attractive. However, the release of dredged sediments, even not contaminated, may affect the environment by increasing the turbidity in water or burying biological habitats. Thus, understanding of the fate of dredged-sediment releases is needed for the management of estuarine and coastal zones.

The process of dredged-sediment release generally passes by three different steps [1]: (i) convective descent during which the sediment cloud falls under gravity (ii) dynamic collapse, occurring when the descending cloud impacts the bottom (iii) transport-dispersion, starting when the sediment transport and spreading are determined more by ambient currents and turbulence than by the dynamics of the disposal operation. Ruggaber [2], and later Bush et al. [3] have studied the convective descent step of sediment release in homogeneous and stratified quiescent water. The

authors consider that, during the convective descent step, particle clouds behave similarly to classic thermals and buoyant vortex rings. They address a complete review of existing studies related to thermals and vortex rings under both homogeneous and stratified conditions. Once having performed a series of experiments during the convective descent step, Ruggaber [2] concludes that: (i) non-cohesive particle clouds evolve by asymptotic deceleration (their settling velocity w is proportional to $t^{-1/2}$) and linear growth rates of cloud radius is similar to classical thermals; (ii) Fine-grained cohesive particle clouds, containing less than 36% solids (by weight) display thermal-like characters ($w \sim t^{-1/2}$), clouds of sediments within the transition range (36–50% solids) exhibit a hybrid-type behaviour. Particle clouds containing more than 50% solids fall as solid clumps with a constant terminal velocity. Bush et al. [3] performed experiments with 11 types of glass spheres of different diameters and densities. They show the typical evolution of particle clouds in a homogeneous ambient. After particle releasing, the thermal shape appears and persists until the particles fall out of the cloud bottom in form of a bowl-shaped swarm. The authors interpret the formation of a bowl-shape swarm as resulting from the interaction between the vortical flow inside the particle cloud and the dense suspended sediments. In agreement with Ruggaber [2], Bush et al.'s [3] experimental results distinguish two stages in the convective descent of a particle cloud: the thermal stage, in which the position of the cloud bottom is proportional to $t^{1/2}$ and the settling velocity of the cloud is

---

* Corresponding author. Tel.: +33 1 30 87 80 79.

E-mail addresses: duc-hau.nguyen@unicaen.fr (D.H. Nguyen), florence.levy@developpement-durable.gouv.fr (F. Levy), damien.pham-van-bang@developpement-durable.gouv.fr (D. Pham Van Bang), sylvain.guillou@unicaen.fr (S. Guillou), kimdan_nguyen@yahoo.fr (K.D. Nguyen), julien.chauchat@grenoble-inp.fr (J. Chauchat).

proportional to $t^{-1/2}$; and the swarm stage, in which the position of the cloud bottom is proportional to t and the settling velocity of the particle cloud is equal to particle fall velocity.

Gensheimer [4] performed flow visualisation experiments in a glass-walled recirculating open channel to study the dynamics of particle clouds released into water with ambient currents. Such particle clouds exhibit three regimes of behaviours, which depend upon the strength of the ambient currents: weak, transitional or strong. In weak ambient currents, particle clouds are advected downstream with a velocity equal to the ambient current, but the behaviour and structure is similar to that in quiescent ambient: the vortex rings form at a similar depth and grow to a similar size. In transitional currents, there is a delay and a distortion of vortex ring formation. In strong currents, vortex rings never form and the coherency of particle clouds is destroyed. Gensheimer [4] studied threshold values to distinguish between the three regimes and showed that these values are dependent upon particle sizes.

Hallworth et al. [5] and Hogg et al. [6] performed instantaneous and sustained releases of saline and particle-laden fluid into an open water flume with and without ambient currents. The distribution of deposited particles as well as their dispersion-transport on the flume bottom were studied. Hallworth et al. [5] and Hogg et al. [6] showed that when there is no ambient current, the density currents spread symmetrically away from the particle source. The propagation velocity decreases as particles settle out of suspension, and therefore reduce the density difference, which drives the density currents. Also they remark that: (i) increasing the initial solid concentration increases the propagation speed and (ii) varying the size of particles in suspension while maintaining the same initial concentration and solid volume flux does not affect the rate of spreading initially.

Villaret et al. [7,8] and Boutin [9] led experiments of sand and mud particle releases in an open water flume with and without ambient currents. These experiments can be considered as 2-D configuration ones (which is not the case of the experiments of [5,6]). A series of tests with different initial solid concentrations, particle sizes, and ambient current strengths was performed. The authors measured: (i) the radius of the particle cloud during the convective descent step as well as the duration of this step (falling time) and (ii) the thickness and velocity of the density current on the bottom.

Accurate predictions on the fate of sediment clouds are needed to help stakeholders in decision making for sustainable development benefits. The different existing tools for dredged-sediment releases can be classified in twofold: analytical [10] or [11] and numerical tools [11–13] or [14]. Analytical tools are usually limited since they result from very restrictive assumptions such as sustainable sediment sources, quiescent water, or Boussinesq approximation. Moreover, they require empirical parameters such as water turbulent entrainment by the sediment cloud or virtual origin of the release. The above-mentioned numerical tools are more adequate for unsteady situations or non-Boussinesq situations. They are single-phase models and based on the passive-scalar hypothesis. This hypothesis stipulates that the solid particles move at the same speed as the fluid ones, except for the vertical component of velocity. Consequently, empirical coefficients in *ad hoc* functions are needed to provide predictions, whose validity is limited to the first step only, *i.e.* the convective descent of the sediment cloud.

Previous numerical studies have shown the limits of the passive-scalar approach in simulating dredged-sediment release. These limits are due to the very high concentration of the sediment cloud. Li [12] used a 3-D single-phase finite-difference model, which is based on solving the Navier–Stokes equations coupled with a sediment transport one, to simulate the convective descent step of particle clouds into quiescent water. Li's [12] model failed to produce the double-peak density distribution and the vortex rings for dense solid concentration. In recent works, Farout-Fréson

[14] used a bi-specie model, which is based on a degeneration of the two-phase model and considers the sediment–water mixture. Interesting results were obtained for the convective-descent step whereas the sediment cloud impact and propagation on the bottom still remained problematic.

Two-phase flow modelling is commonly used in many industries such as chemical, nuclear or pharmaceutical industries. Recently, it was applied to simulate the sediment transport in free surface and non-hydrostatic flows [15–20]. In the two-phase flow modelling, the computing domain is extended to the true non-erodible bed, *i.e.* no extra-Consolidation and Sedimentation Bed (CSB) Model is needed (see [19]). The continuity and motion equations are solved for both fluid and solid phases, with interaction terms between them. A non-Newtonian rheology for sediment-laden flows and non-Boussinesq situations can be accounted for, which is crucial for dense particle-laden flows.

The purpose of this paper is to present the applicability and the relevance of the two-phase approach in simulating tests of dredged-sediment release into open waters, obtained from a large physical model testing facility by Villaret et al. [7,8] and Boutin [9]. Section 2 briefly describes the mathematical and numerical background of the two-phase model. The experimental data are presented in Section 3. Simulation results on the dredged-sediment release process are discussed in Section 4. Finally, Section 5 explores the prospects for developing and improving two-phase models of sediment transport.

2. Model description

In the present two-phase flow model, the Eulerian–Eulerian description is used for the fluid–solid particles system. Starting from the Navier–Stokes equations, we strictly apply the mathematical treatment from Drew and Lahey [21] to obtain the governing equations (mass conservation and momentum conservation) for the continuous- (water) and the dispersed- (solid particles) phases. Herein we briefly recall the basic equations with special closure laws.

2.1. Governing equations

For each phase, we consider the conservation Eq. (1) with the subscript k to specify the phase of consideration: k is replaced by f or s for the fluid or the sediment phase, respectively

$$
\begin{cases}
\frac{\partial(\alpha_k \rho_k)}{\partial t} + \vec{\nabla} \cdot (\alpha_k \rho_k \vec{u}_k) = 0 \\
\frac{\partial(\alpha_k \rho_k \vec{u}_k)}{\partial t} + \vec{\nabla} \cdot (\alpha_k \rho_k \vec{u}_f \otimes \vec{u}_f) = \vec{\nabla} \cdot \left(\alpha_k \left(-p_k \overline{\overline{I}} + \overline{\overline{\tau}}_k + \overline{\overline{\tau}}_k^{Re} \right) \right) + \alpha_k \rho_k \vec{g} + \vec{M}_k
\end{cases}
\tag{1}
$$

where α_k, $\vec{u}_k$ and ρ_k stand for the volume fraction, velocity and density of phase k respectively, $\vec{g}$ is the acceleration of gravity, $\vec{M}_k$ is the inter-phase momentum transfer, p_k is the pressure of phase k, $\overline{\overline{\tau}}_k$ and $\overline{\overline{\tau}}_k^{Re}$ are the viscous and Reynolds stress tensor, respectively. $\overline{\overline{I}}$ is the identity matrix.

The sum of volume fractions, α_s, is obviously equal to 1. In the present model, the viscous stress tensor, $\overline{\overline{\tau}}_k$, is considered as a function of shear rate tensors, $\overline{\overline{D}}_k$. These functions are presented in Eq. (2) by Lundgren [22]. Both shear rates, $\overline{\overline{D}}_s$ and $\overline{\overline{D}}_f$, are involved in computing of fluid and solid viscous stresses via viscosity coefficients μ_{ff}, μ_{fs}, μ_{sf} and μ_{ss} given by Eq. (3)

$$
\alpha_f \overline{\overline{\tau}}_f = \mu_{fs} \overline{\overline{D}}_s + \mu_{ff} \overline{\overline{D}}_f, \quad \alpha_s \overline{\overline{\tau}}_s = \mu_{ss} \overline{\overline{D}}_s + \mu_{sf} \overline{\overline{D}}_f
\tag{2}
$$

$$
\mu_{ff} = \alpha_f \mu_f, \quad \mu_{fs} = \alpha_s \mu_f, \quad \mu_{ss} = \alpha_s \beta \mu_{fs}, \quad \mu_{sf} = \alpha_s \beta \mu_{ff}
\tag{3}
$$

It is worth noting that viscosity coefficients used for the solid stress, μ_{sf} and μ_{ss}, are weighted by an amplification factor β which accounts for the non-Newtonian behaviour of the sediment mixture. We consider the model proposed by Graham [23], relating the inter-particle distance, ξ normalised by the sediment diameter d, (or the sediment concentration), to the amplification factor, β

$$\beta = \frac{5}{2} + \frac{9}{4}\left(\frac{1}{1+\xi/d}\right)\left[\frac{1}{2\xi/d} - \frac{1}{1+2\xi/d} - \frac{1}{(1+2\xi/d)^2}\right]\frac{1}{\alpha_s} \qquad (4)$$

with

$$\xi/d = \frac{1 - (\alpha_s/\alpha_{s,\max})^{1/3}}{(\alpha_s/\alpha_{s,\max})^{1/3}} \qquad (5)$$

where $\alpha_{s,\max}$ is the maximum close packing concentration, which value is equal to 0.625 for non-cohesive spherical and mono-dispersed solid particles [23].

The $\vec{M}_k$ term acting in the right hand side of motion Eq. (1) refers to the momentum transfer between the two phases. As detailed in Eq. (6), this term is decomposed into two components: the jump conditions (p_{ki} and $\overline{\overline{\tau_{ki}}}$) at the solid–liquid interface and the different forces ($\vec{M}'_k$) acting on phase k such as drag, lift or added mass forces

$$\vec{M}_f = p_{fi}\vec{\nabla}\alpha_f - \overline{\overline{\tau_{fi}}}\vec{\nabla}\alpha_f + \vec{M}'_f, \quad \vec{M}_s = p_{si}\vec{\nabla}\alpha_s - \overline{\overline{\tau_{si}}}\vec{\nabla}\alpha_s + \vec{M}'_s,$$
$$\vec{M}'_f = -\vec{M}'_s \qquad (6)$$

For the system of interest, no discontinuity of pressure and shear stress is considered across the interface (Eq. (7)). The drag force is assumed to be dominant in the $\vec{M}'_k$ term as argued by Hsu et al. [24] (Eq. (8)).

$$p_{fi} = p_f - \frac{\rho_f}{4}\|\vec{u}_f - \vec{u}_s\|^2, \quad p_{si} = p_{fi}, \quad \overline{\overline{\tau_{si}}} = \overline{\overline{\tau_{fi}}} = \beta\overline{\overline{\tau_f}} \qquad (7)$$

$$\vec{M}'_s \approx \vec{F}_D = \frac{\alpha_s\rho_s}{\tau_{fs}}\vec{u}_r, \quad \tau_{fs} = \frac{4d\rho_s}{3\rho_f C_D\|\vec{u}_r\|}, \quad C_D = \frac{24}{\mathrm{Re}_s}f(\mathrm{Re}_s,\psi) \qquad (8)$$

This last equation expresses the drag force as a function of the solid concentration (α_s), the relaxation time of solid particles (τ_{fs}) and the velocity lag ($\vec{u}_r$) between fluid and solid particles. The particle relaxation time is fundamental in two-phase flow theory as it is used to define the Stokes number and the separation between one-, two- or four-way coupling [25]. It is computed from the drag coefficient (C_D), which depends on the particle Reynolds number and on the shape function (ψ) of sediment particles (here we take $\psi = 1$). The drag coefficient formula by Haider and Levenspiel [26] is used in the present study.

2.2. Numerical technique

The techniques developed by Guillou et al. [27] are used to solve the system of Eq. (1). A projection technique [28] is applied to calculate the pressure and velocity for each phase. The σ-transformation is applied to the vertical coordinate in order to fit the computing mesh to the free surface evolution. Spatial derivatives are approximated by the second-order finite volume method. The time scheme is implicit in the vertical direction and explicit in horizontal one. Advection terms in Eq. (1) have been handled by either hybrid or TVD schemes. The resulting linear equation system is solved by the GMRES or Gauss–Seidel methods. A staggered grid is used to avoid the spurious oscillations induced by the projection technique [29].

3. Experimental data

Physical model testing of sediment releases was performed at EDF LNHE [7–9]. A large hydraulic facility (straight channel, 72 m long, 1.5 m wide, 1.5 m maximum height) is used and the three steps experienced during a sediment-release test are recorded: (i) the convective descent of the sediment cloud; (ii) the sediment-cloud impact on the bottom with the generation of density currents; (iii) the propagation of density currents up- and down-stream until the equilibrium under ambient current. A special device was designed to release the sediment mixture (initially prepared at given concentrations). Villaret et al. [7,8] used pure sand and sandy mud, while Boutin [9] worked with pure mud. Here, we restrict our study to the pure-sand case. The experimental set-up has an aspect ratio, width over flow depth, of one and a half with side-walls made of glass. The friction on the side-walls is rather low and even if the channel can not be considered as wide (aspect ratio greater than 10), the flow can reasonably be considered as two dimensional. The measurement zone is located in the central part of the channel, thus far from the boundaries.

A specifically designed recipient (maximum capacity of 60 L) is placed at 17 cm below the free surface: its opening is computer-controlled and synchronised with a camera that takes pictures every 0.5 s. Concentration measurements are also obtained using OPCON optical transducers, but only at three fixed points (Fig. 1a). As the duration of the convective descent stage is extremely short (about 0.7–1.8 s), it is very difficult to capture accurately the moment when the sediment cloud impacts the bottom.

First, the ambient current is imposed by measured velocities. Then the mixture of sand and water is placed in the recipient at a desired concentration. Finally, the computer-aided procedure starts: the bottom of the recipient is suddenly opened (Fig. 1b) and simultaneously picture acquisitions and concentration measurements begin.

Eleven tests were performed using the previously detailed protocol. Table 1 gives the different testing conditions. In the pure-sand experiments, two different sediment diameters (D_p), sediment-release volumes (V_d), and initial concentrations of the mixture (C_m) were used in order to investigate their individual and collective influence. The injection velocity (W_0) could not be controlled in the experiments. It was estimated by Villaret et al. [7,8] using Krishnappan's semi-empirical model [11]. The parameters involved in the latter are the densities (fluid and solid), the released volume of sediments, the injection radius, as well as empirical coefficients depending on the grain size, the densities and the viscosity of the ambient medium.

Using the pictures and the measurements of concentrations at three fixed positions (Fig. 1a), Villaret et al. [7,8] determine the following parameters: (1) the falling time (time lapse between the release of sediments and the impact of the sediment cloud on the bottom), (2) the up- and down-stream (R_u, R_d) radius of the cloud, (3) the maximum height of the density current, (4) the front velocity of the density current. The uncertainties on the cloud radius (2.5 cm as estimated by Villaret et al. [7,8]) and on the falling time (0.5 s as estimated by Villaret et al. [7,8]), are explained by the metric scale and by the rapidity of the phenomenon, respectively. These parameters provide a basis for comparisons between the numerical and experimental studies.

4. Numerical studies

The 2-D X/Z computation domain covers 14 m in the horizontal direction and 1 m in the vertical one. The lateral boundaries are transparently open to avoid reflections. As no free surface movement is video-recorded during experiments, the surface is assumed
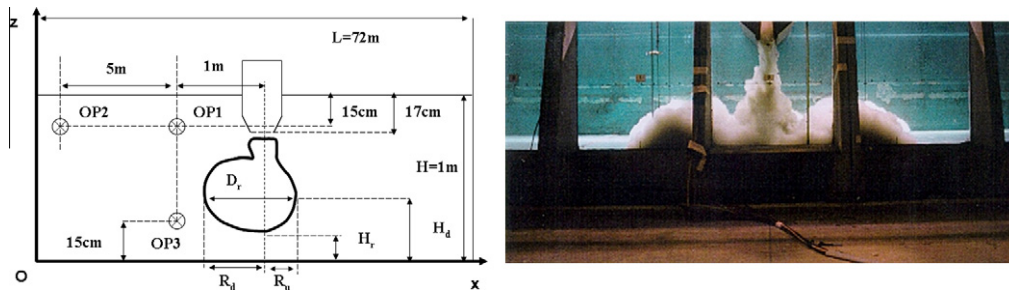
Fig. 1. Definition sketch: (left) location of Optical Probes (OP) for turbidity measurements; (right) sediment release [9].

Table 1
Testing conditions and nomenclature: W_0 is the injection velocity from the recipient, D_p the sediment particle diameter, ρ the dry density of the solid, C_m is concentration of the mixture, V_d the volume of dumped material, U_c the ambient velocity (from Villaret et al. [7,8]).

Tests	W_0 (m/s)	D_p (µm)	ρ (kg/m³)	C_m (g/L)	V_d (L)	U_c (m/s)
e6	0.60	90	2650	350	45	0
e11	0.79	90	2650	450	60	0
e12	0.89	160	2650	450	60	0
e13	0.79	90	2650	450	60	0.10
e14	0.89	160	2650	450	60	0.10
e15	0.79	90	2650	450	60	0.20
e16	0.89	160	2650	450	60	0.20
e17	0.79	160	2650	450	60	0.15
e18	0.89	90	2650	450	60	0.15
e19	0.79	160	2650	450	60	0.25
e20	0.89	90	2650	450	60	0.25

to be rigid. The sediment recipient is located 17 cm below the water surface. The condition at the bottom corresponds to an impermeable condition. More important is the boundary condition at the injection device, where we should impose a flux of solid mass and profiles for the solid and fluid vertical velocities. The injection velocity profile was not controlled in experiments [7,8], and velocity measurements are missing near the sediment recipient. For numerical simulation, a velocity profile is required and we remark that the calculated falling time of particles and sediment-cloud radius are sensitive enough to the choice of this profile. By trials and errors, we conclude that a Poiseuille-type profile as follows is well-suited to the experimental conditions:

$$W_{inj} = W_0 \left(1 - \frac{x^2}{R_{inj}^2} \right)$$

where W_0 is the averaged vertical injection velocity proposed by Villaret et al. [7,8] (Table 1), R_{inj} is the half of the recipient-bottom opening and x is the distance from the vertical axis of the recipient.

4.1. Justification of the two-phase model use

Most of the physical processes involved in sediment transport can be accounted for by two-phase approaches, provided that relevant closure laws are given for Eq. (1). This closure issue needs to be handled carefully for the model to be consistent with the physical processes at work in the studied phenomenon. Also, two-phase numerical models are highly CPU time consuming compared with single-phase ones (classical sediment transport model based on a passive-scalar hypothesis for the sediment phase). Therefore, the use of a two-phase sediment transport model against a single-phase one for any sediment transport problem must be justified by the fact that the latter is not able to simulate the problem satisfactorily. In order to justify the use of a two-phase model for dredged sediment release simulation, we make a comparative

study of the results from single- and two-phase models. This comparison is performed on the basis of test e12's parameters (Table 1) but with a slightly different geometrical configuration, with a sediment injection 15 cm below the surface instead of 17 cm for test e12. We point out that all other parameters are identical for the single-phase and two-phase simulation.

The governing equations for a single-phase model are:

$$\begin{cases} \vec{\nabla} \cdot \vec{u}_f = 0 \\ \frac{\partial(\rho \vec{u}_f)}{\partial t} + \vec{\nabla} \cdot (\rho \vec{u}_f \otimes \vec{u}_f) = \vec{\nabla} \cdot \left(-p\overset{\Rightarrow}{I} + \overset{\Rightarrow}{\tau} + \overset{\Rightarrow}{\tau}^{Re} \right) + \rho \vec{g} \\ \frac{\partial(\rho_s \alpha_s)}{\partial t} + \vec{\nabla} \cdot (\rho_s \alpha_s \vec{u}_s) = 0 \\ \text{with} \begin{cases} \vec{u}_s = (u_f, w_f - w_{sett}) \\ \rho = \rho_s \alpha_s + \rho_f(1 - \alpha_s) \end{cases} \end{cases} \quad (9)$$

In Eq. (9), w_{sett} is the solid-particle settling velocity, which depends on the particle size, the particle-Reynolds number, and the solid-particle concentration. u_k and w_k are the horizontal and vertical components of the velocity of phase k, respectively. The only forcing in Eq. (9) is buoyancy. No interaction between fluid and solid particles neither between solid and solid particles is taken into consideration in a single-phase model.

The computed domain, which is here 6 m long and 1 m high, is discretised by a computing grid of 0.5×0.5 cm resolution and by a time step of 5×10^{-4} s. In Fig. 2, the maximum value of vertical-velocity lag $-w_{sett} = w_s - w_f$ obtained by the two-phase model is around 1.5–2.0 cm s^{-1}. This is in very good agreement with the settling-velocity value of 1.8 cm s^{-1} given by Van Rijn's formulas for sand particles of 80 µm radius [6,7]. Table 2 shows results obtained by the single-phase and two-phase models for the falling time and the radius of the sediment cloud at the moment of its impact on the bottom. The single-phase model predicts a cloud radius larger
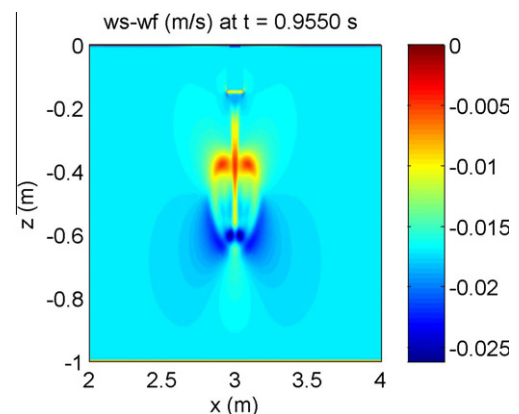

Fig. 2. Isocontour map of the vertical-velocity lag between the fluid and solid phases ($w_s - w_f = -w_{sett}$).

Table 2
Parameters of the convective descent stage of the dredged-sediment release.

	Falling time (s)	Radius (cm)
Single-phase model	1.41	31
Two-phase model	1.41	25

than the one given by the two-phase model. The falling time of 1.41 s given by the two-phase model without any parameter tuning is of the same order of magnitude as what is observed in experiments. With the single-phase model, such a falling time can only be obtained by forcing the settling velocity w_{sett} (in Eq. (9)) up to a value of 36 cm s^{-1}, which is physically aberrant.

Fig. 3 plots the iso-contours of turbidity and vorticity calculated by the two-phase model (left) and the single-phase one (right). The properties of the sediment cloud calculated by both models are different. The two-phase model predicts a double-peak turbidity distribution, *i.e.* the sediment cloud is divided into two cores, which are symmetrical and distanced from a central axis (Fig. 3, upper-left). These two symmetrical cores were discussed by Maxworthy [30] for turbulent vortex rings, formed by pushing a fluid mass through a hole into another ambient fluid. This has a certain similarity with the present test. The author found that the distance between the two cores depends on the diameter of the hole, on the vertical distance travelled by the vortex ring, and on the Reynolds number. The single-phase model fails to reproduce this phenomenon: only one turbidity core is detected (Fig. 3, upper-right). The same turbidity distribution was obtained by Li [12], using a

single-phase model for a case with a large settling velocity (14 cm s^{-1}). An explanation to this turbidity distribution can be found in vorticity maps. Indeed in Fig. 3 (lower-right), at the location of the sediment cloud calculated by the single-phase model, *i.e.* for $z < -0.6$ m, the vorticity value is zero everywhere. No recirculation occurs there, and consequently the sediment cloud is not separated. Fig. 3 (lower-left) presents a completely different physical pattern: inside the sediment cloud, vortex rings are reproduced by the two-phase model with two distinguished recirculation zones, which are cyclonic (on the right of the central axis) and anti-cyclonic (on the left). These vortex rings separate the sediment cloud into two zones with a core for each, as above-mentioned. Clearly, the two-phase model which takes into consideration the fluid–solid and solid–solid interactions, is able to correctly simulate the convective descent of dredged-sediment release, whereas a single-phase model fails to do so. This justify the use of a two-phase model against a single-phase one in this case.

4.2. Simulation and results

Numerical modelling was performed for all tests described in Table 1. Tests e06, e11 and e12 are without ambient currents, while the others are with ambient currents. The computed domain, which is 14 m long and 1 m high, is discretised by a 1.0×1.5 cm computing grid. The time step is 10^{-3} s. Below we present and discuss the numerical results for the convective descent of the sediment cloud, as well as for the formation and propagation of density currents on the bottom.
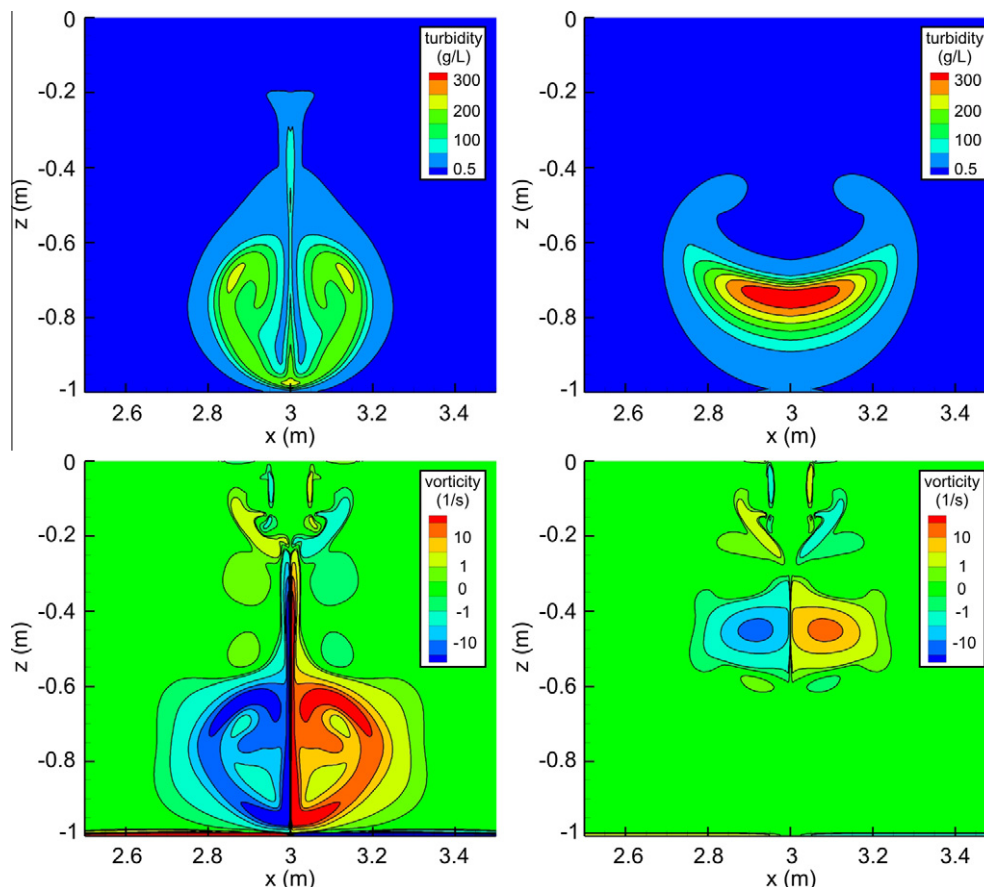

Fig. 3. Isocontour maps of turbidity (top) and vorticity (bottom) at the impact of the sediment cloud on the bottom, calculated using the two-phase model (left) and the single-phase one (right).

Table 3
Parameters of the convective descent stage of the dredged-sediment release for tests e06, e11 and e12.

	Falling time (s)		Radius (cm)	
	Numerical	Experimental	Numerical	Experimental
Test e06	1.8	1.76 (1.26–2.26)	27	29 (26.5–31.5)
Test e11	1.5	0.95 (0.45–1.45)	34	32 (29.5–34.5)
Test e12	1.3	0.72 (0.22–1.22)	27	28 (25.5–30.5)

4.2.1. Convective descent of the sediment cloud

4.2.1.1. Without ambient current. Table 3 compares, for tests e06, e11 and e12 of sediment release in quiescent water, experimental and two-phase results for the falling time and the sediment-cloud radius at the moment of the impact on the bottom. Considering the uncertainty on experimental measurements, the numerical results are satisfying, with a slight overestimation of the falling time for tests e11 and e12.

Fig. 4 plots the evolution of the position of the cloud bottom with respect to the injection depth ($Z_r = 0.83 - H_r$, see Fig. 1 for notations) computed by the two-phase model for tests e06, e11 and e12. A threshold turbidity value of $0.5\,\mathrm{g\,L^{-1}}$ is used to determine the cloud geometry (as suggested by Farout-Fréson [14]). Numerical results for these tests confirm Bush et al.'s [3]

observations: during the convective descent, there are two distinct stages: a thermal stage, in which the evolution of Z_r is proportional to $t^{1/2}$ and a swarm stage, in which Z_r is linear to t.

Fig. 5 presents the simulation results for test e12 at different times (1.0 s, 1.3 s; 2.6 s and 4.0 s). The particle release generates the motion of two vortex rings, which are cyclonic and anti-cyclonic. During the lateral expansion of the particle cloud, numerical results illustrate the entrainment of surrounding water into the rear of the cloud, which is consistent with the physical interpretation of Morton et al. [10]. This shows that the horizontal component of fluid- and solid-velocities is unequal in direction and magnitude.

4.2.1.2. With ambient current. Fig. 6 presents numerical results for test e19 with an ambient current. Following Gensheimer [4], this case exhibits a character of transitional regime. Indeed, Fig. 6 shows a distortion of the particle cloud. We note that the cloud shape is similar to that described by Hogg et al. [6], based on experimental observations: the downstream branch of the cloud is more diffuse than the upstream one, which displays a wedge shape. The zone of maximum concentration (red colour in Fig. 6) is localised rather on the right side of the cloud, *i.e.* in its upstream part. The impact of particle clouds on the bottom is delayed by ambient currents. The stronger the ambient current is, the more delayed the
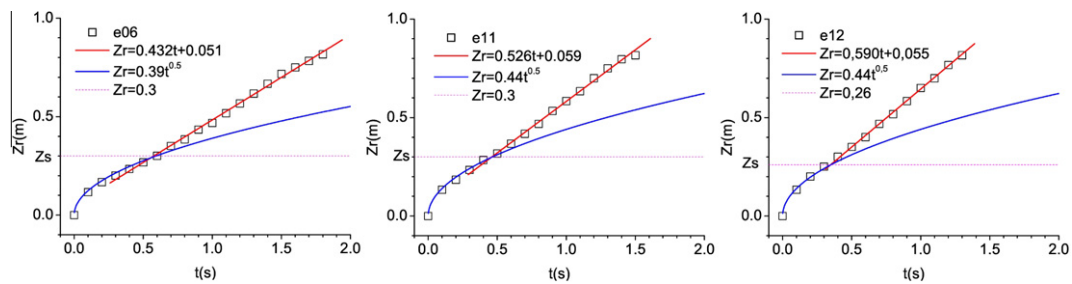

Fig. 4. Evolution of the position of the cloud bottom, $Z_r = 0.83 - H_r$ (see Fig. 1) computed by the two-phase model, without ambient current.
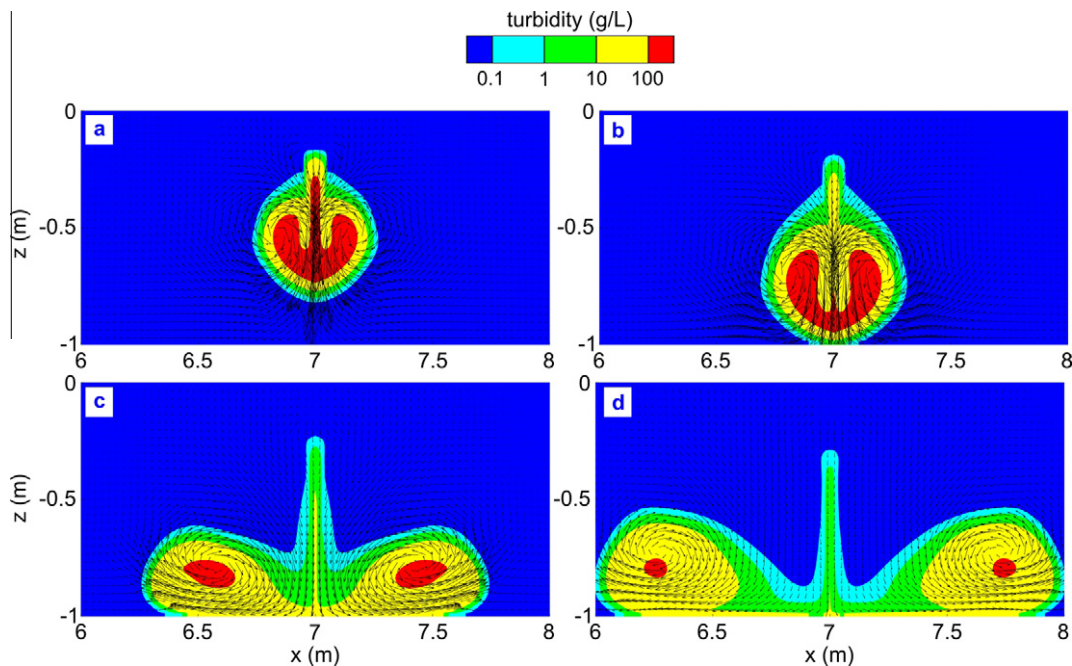

Fig. 5. Particle cloud evolution and development of two cyclonic and anti-cyclonic vortices (test e12, without ambient current). Colours represent the turbidity and vectors give the solid-phase velocity at: (a) 1 s; (b) 1.3 s; (c) 2.6 s and (d) 4.0 s. (For interpretation of the references to colour in this figure legend, the reader is referred to the web version of this article.)
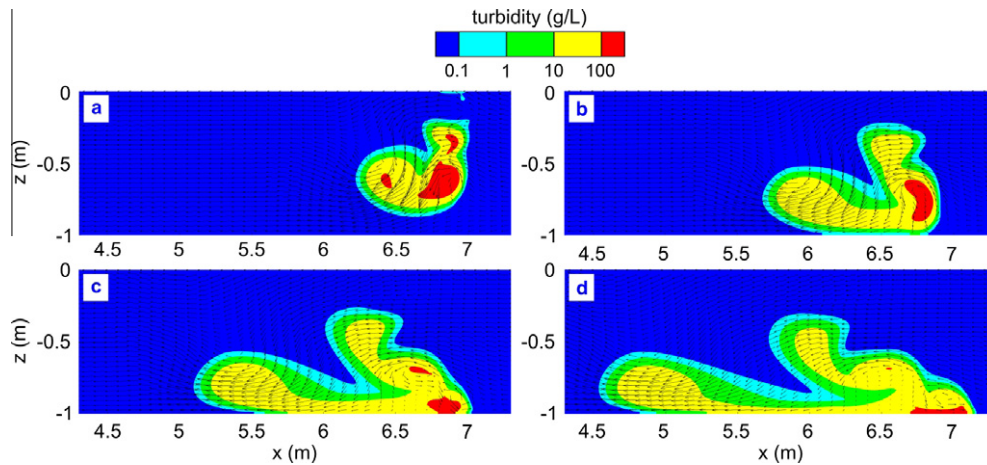
Fig. 6. Simulation results for test e19 with an ambient current of 25 cm s^{-1} (flow direction from right to left) at: (a) 1.5 s; (b) 2.5 s; (c) 3.5 s and (d) 4.5 s. Colours represent the turbidity, vectors give the solid-phase velocity field. (For interpretation of the references to colour in this figure legend, the reader is referred to the web version of this article.)

impact on the bottom is. This is well-illustrated by comparing tests e12, e14 and e16, for which all parameters are equal except the intensity of the ambient current. The calculated falling time is 1.3 s for test e12 with no ambient current, 1.9 s for test e14 with a current velocity of 0.1 m s^{-1}, and 2.3 s for test e16 with a current velocity of 0.2 m s^{-1}.

Fig. 7 plots the R–H_r relationship for all the tests with or without ambient currents, where H_r is defined in Fig. 1. This figure confirms the loss of symmetry of particle clouds when there is an ambient current and the accentuation of this tendency when the intensity of the ambient current increases. The longitudinal coordinate of centroid (R) is obviously larger for higher ambient velocities, which is in agreement with Gensheimer [4].

4.2.2. Density current formation and propagation on the bottom

The impact of the sediment cloud on the bottom generates a density current, which simultaneously propagates on the bottom

and takes part in sedimentation processes. The propagation of the density current is analysed through two parameters: its height and its spreading rate.

Fig. 8 presents the time evolution of the maximum height of the density current calculated for tests e06 and e11 [7,8]. These results show that for both tests: (i) this height reaches its maximum value around 5 s after the sediment release; (ii) there are no large differences (<5 cm) between the maximal and stabilised values of this height. The maximum height of the current observed in experiments is also shown in Fig. 8. Unfortunately, for each experiment, the height was measured only at one given location, at probe OP3 (*i.e.* at a horizontal distance of 1 m from the injection device). We note however that the calculated and observed heights are of the same order of magnitude.

Fig. 9 shows the position of the front of the density current as a function of time for tests e06, e11 and e12 (quiescent water). Clearly, in all these tests the propagation is symmetric and linear
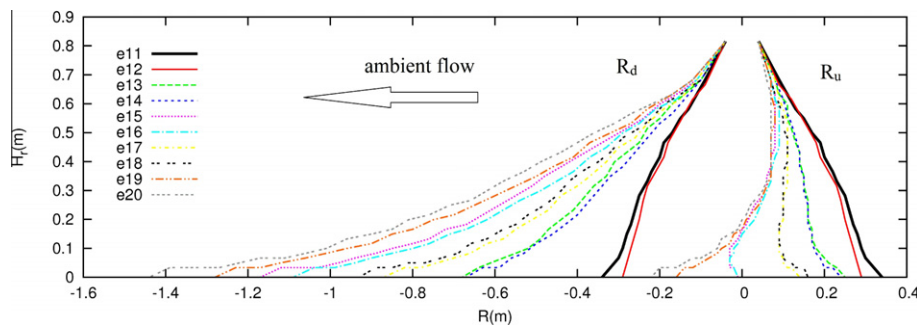

Fig. 7. Height H_r *versus* the up- and down-stream radius R_u, R_d respectively for the convective descent stage. Definition of H_r, R_u and R_d are given in Fig. 1.
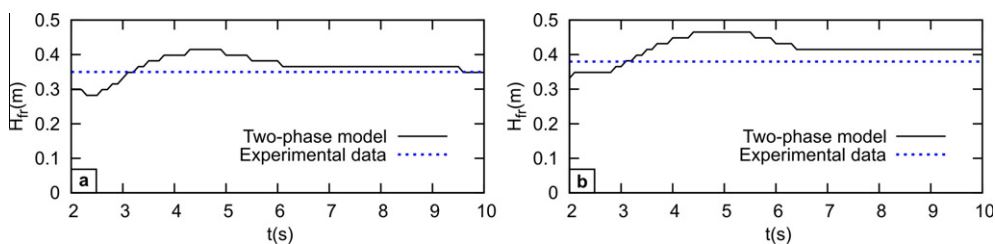

Fig. 8. Time evolution of the maximum height of the density current during its propagation on the bottom calculated by the two-phase model for (a) test e06 and (b) test e11. The maximum height measured in experiments at OP3 is indicated in dashed lines.
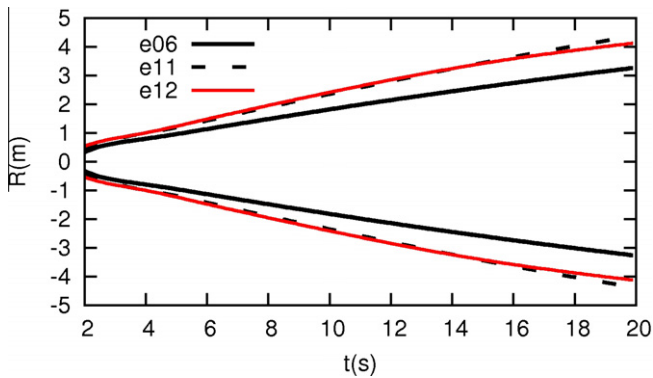
Fig. 9. Position of the front of the density currents as a function of time.

for a short time (20 s). However, the $R \sim t$ relation would certainly become more curved for a longer time. The spreading rates should reduce with time because particles settle, reducing the density contrast that drives the motion. As mentioned by Hogg et al. [6], the spreading rate is highly influenced by the density current concentration. This is observed by comparing tests e06 and e11 which differ only by their initial solid concentration and released volume (350 g L^{-1} and 45 L respectively for e06 compared with 450 g L^{-1} and 60 L for e11, see Table 1). The influence of particle size is also perceptible, but for longer times. Larger particles settle out of suspension faster than finer ones, and therefore reduce density differences and spreading rates faster [6]. Fig. 10 shows the time evolution of the front velocity of the density current for tests e11 to e20. For both particle size groups (group I: $D_p = 90$ μm {e11; e13; e15; e18; e20} and group II: $D_p = 160$ μm {e12; e14; e16; e17; e19}), propagation velocities on the bottom U_{fr} reduce as time increases. At $t = 25$ s, U_{fr} of group II ($D_p = 160$ μm) tends to be less than that of group I ($D_p = 90$ μm). For example, at this moment the propagation velocity is 0.1 m s^{-1} for test e12 ($D_p = 160$ μm and $W_0 = 0.89$ m s^{-1}) while it is 0.16 m s^{-1} for test e11 ($D_p = 90$ μm and $W_0 = 0.79$ m s^{-1}). We note that the influence of the injection velocity is no more perceptible. The dominant parameter at this stage seems to be the particle size, however there are no couple of experiments for which only the particle size is changed and it is therefore not possible to conclude on this point.

As the convective descent step is very short (<1.80 s), the time uncertainty as well as the random drop of sediments from the recipient in experiments do not allow us to compare in a satisfying way pictures with numerical results at this step. We can only make comparisons at the step of sediment propagation on the bottom. Fig. 11 compares, for test e12, a picture taken at $t = 3.68$ s [8] with numerical results at two instants, $t = 3.70$ s and 4.20 s, which are shifted by 0.5 s. The interval between these two instants corresponds to the time uncertainty of measurements [8].

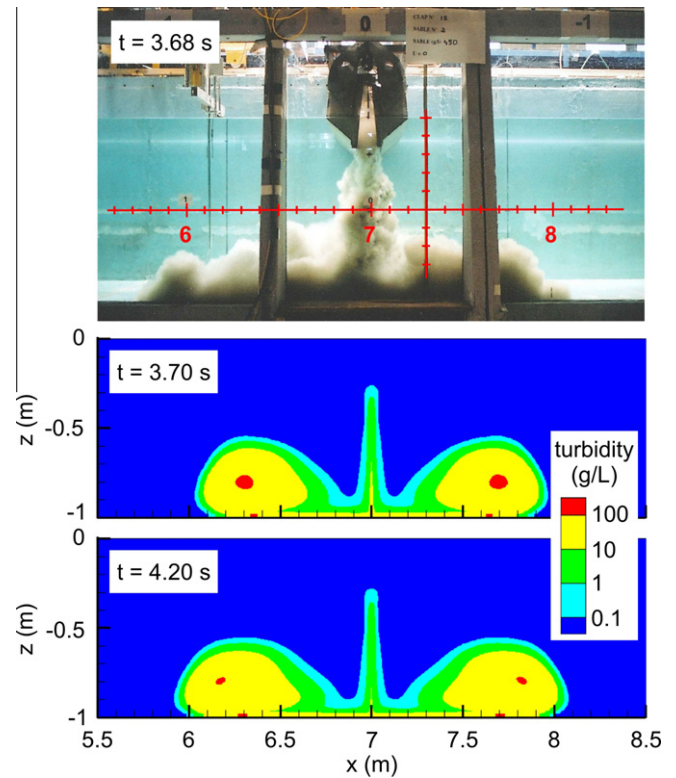**Fig. 11.** Comparison between an experimental observation and the numerical results for test e12: (a) picture taken at $t = 3.68$ s by Villaret et al. [8]; (b) sediment cloud calculated at $t = 3.70$ s; and (c) sediment cloud calculated at $t = 4.20$ s.

We note that the sediment propagation on the bottom is not perfectly symmetric on the picture. This can be explained by the fact that, in the experiments, insuring a symmetric sediment release from the recipient was very difficult. This asymmetry disturbs experimental results, and then could be responsible for slight differences between the experimental data and the numerical results. If we only consider the right part (from the vertical axis) of the density current, a good enough agreement between the numerical and experimental results is obtained, in particular for the density–current right end, which is located around $x = 8.0$ m. However, we note that the vertical stem of the calculated sediment plume is not as developed as the observed one. Consequently, by mass conservation principle, as the stem width is not widening, the calculated sediment density current develops vertically. At the right end, the height of the calculated current is slightly higher than that observed (0.4 m compared to 0.3 m, respectively). We suspect that the random drop of sediments from the recipient, as well as a local flow that could be generated by opening the
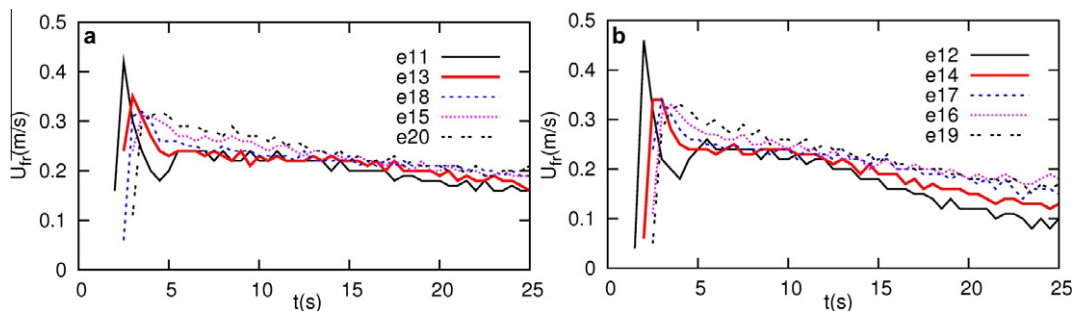

Fig. 10. Propagation velocity U_{fr} of the front of the density current on the bottom for the different particle sizes: (a) (left) group I ($D_p = 90$ μm) and (b) group II ($D_p = 160$ μm).
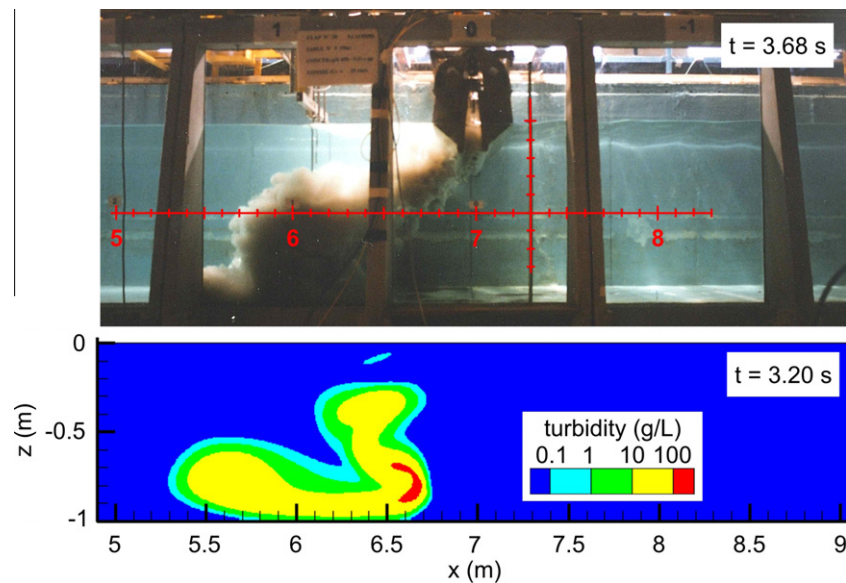
Fig. 12. Comparison between an experimental observation and the numerical result for test e20: (a) picture taken at $t = 3.68$ s by Villaret et al. [8] and (b) sediment cloud calculated at $t = 3.20$ s.

recipient bottom, provoke unexpected fluctuations and develop the stem width. At present, the model does not take into consideration the random drop neither the local flow generated under the recipient bottom.

Fig. 12 compares, for test e20, the picture taken at $t = 3.68$ s [8] with the calculated sediment plume at $t = 3.20$ s. Again, the time shift between the two images corresponds to the experimental time uncertainty. A good enough agreement is obtained, particularly regarding the position of the sediment cloud.

5. Conclusions

This study presents numerical simulation of sediment release with and without ambient currents using a two-phase model. This modelling framework is particularly well-suited to such a test case since fluid and solid phase velocities differ in amplitude and direction. Such a difference could not be captured by classical single-phase numerical modelling based on the passive-tracer assumption.

The numerical results obtained by the model are in correct agreement with the experimental data. For the parameters remaining inaccessible from the experiment such as the concentration field, the formation of counter-rotating vortices or the influence of ambient current, the numerical model provides results that are in qualitative agreement with previously published studies.

The formation and propagation of density currents are also consistent with experiments. One important characteristic and advantage of our two-phase approach is to consider the entire domain, *i.e.* there is no *a priori* layer decomposition to deal with density currents.

In this study, we consider non-cohesive sediments. For such a case, no consolidation or flocculation processes are encountered. To deal with cohesive sediments, closure laws for consolidation should be introduced but more important is the need to account for the flocculation/deflocculation processes that should play a fundamental role in the dynamics of the system during the descent of the sediment cloud.

Some bias (vertical structure of turbidity currents) remains to improve but this information is crucially missing in published data.

Appendix A. Model performance

The performance of the present model is evaluated by analysing the orders of accuracy of numerical schemes in time and in space. Since there does not exist an exact solution for the problem studied here, we use a fine mesh and a small time step to compute a reference solution, and consider this reference solution as the exact solution in estimating the numerical error norms, L_1 and L_2 of the solid velocity.

A.1. Accuracy order in time

We estimate numerical orders of accuracy in time of the present model. The time step dt is successively taken as 1×10^{-3}, 5×10^{-4} and 10^{-4} s. The reference solution has been computed using a 1×1 cm mesh with a time step of 5×10^{-5} s. Fig. 13 plots the variation of L_1 and L_2 errors in comparison with the reference solution at two instants: at $t = 0.955$ s (sediment-cloud position at mid-depth) and $t = 1.4095$ s (sediment cloud nearly impacts the bottom). L_1 and L_2 errors decrease as dt decreases, which proves the consistency of the model. The convergence in time of the present model is obtained with a numerical order varying from 1.10 to 1.27. The numerical order of accuracy is slightly reduced when the sediment cloud impacts the bottom.

A.2. Accuracy order in space

We estimate numerical orders of accuracy in space of the present model. A 0.5×0.5 cm mesh with a time step of 5×10^{-4} s has been used to compute the reference solution. It is necessary to keep in mind that if the space step h was considerably reduced

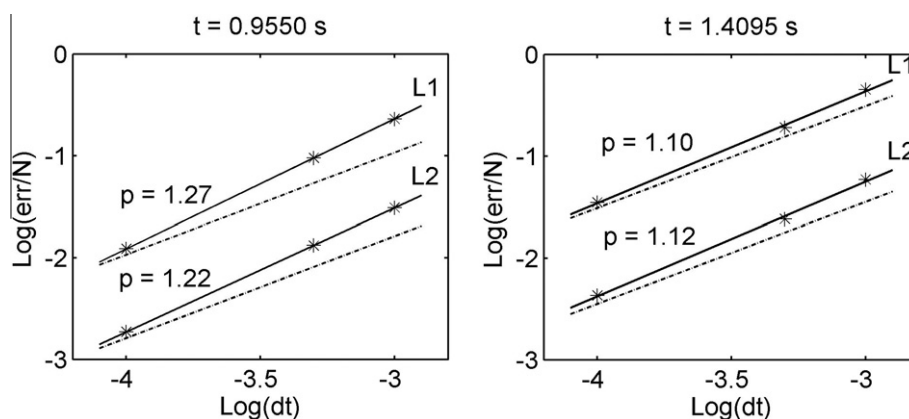**Fig. 13.** Variation of L$_1$ and L$_2$ errors and numerical orders of accuracy in time at $t = 0.955$ s (sediment cloud located at mid-depth) and $t = 1.4095$ s (impact of the sediment cloud on the bottom). Dashed lines indicate an order of accuracy equal to 1.

Fig. 14. Variation of L$_1$ and L$_2$ errors and numerical orders of accuracy in space at $t = 0.955$ s (sediment cloud located at the mid-depth) and $t = 1.4095$ s (impact of the sediment cloud on the bottom). Dashed lines indicate an order of accuracy equal to 1.
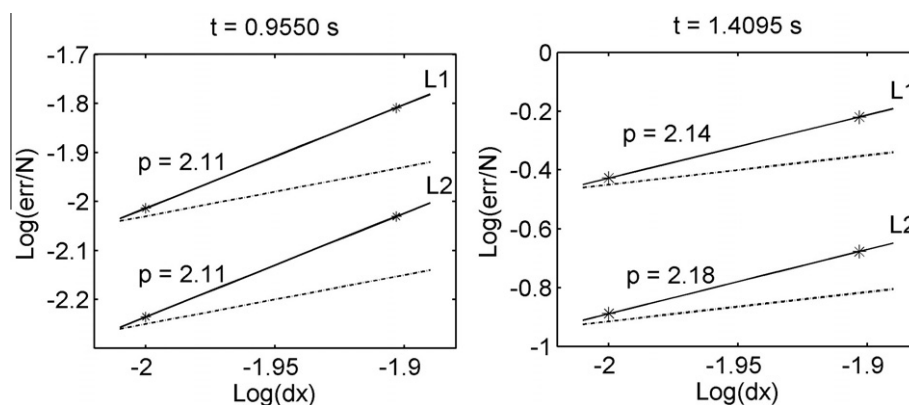
(by 8–10 times, for example), the numerical model could capture fine details of subgrid-scale physical phenomena. However, this is not the scope of this paper: we are only interested in the fate of a dredged-sediment cloud and its impact on the bottom. Therefore, we deliberately do not reduce h so much in comparison with the reference value, $h_{ref} = 0.5$ cm. The space step h is taken as 1.0 and 1.25 cm.

Fig. 14 plots the variation of L$_1$ and L$_2$ errors in comparison with the reference solution at $t = 0.955$ s and $t = 1.4095$ s. Once again, the consistency of the present model is proven. The numerical order of accuracy of the used numerical schemes in space reaches about 2.10–2.20 as expected. Note that the mass conservation is well-respected by the present model as far as the relative solid-mass error is less than 0.005%.

References

[1] Johnson BH, Fong MT. Development and verification of numerical models for predicting the initial fate of dredged material disposed in open water. Report 2: Theoretical Development and verification results, Department of the Army, Waterways Experiment Station, Corps of Engineers, Vicksburg, MS 39180-6199; 1995.

[2] Ruggaber GJ. Dynamics of particle clouds related to open-water sediment disposal. PhD thesis, MIT, Cambridge, MA: Dept. of Civil and Environmental Engineering; 2000. 241p.

[3] Bush JWM, Thurber BA, Blanchette F. Particle clouds in homogeneous and stratified environments. J Fluid Mech 2003;489:29–54.

[4] Gensheimer RJ. Dynamics of particle clouds in ambient currents with application to open-water sediment disposal. Master thesis. MIT, Cambridge, MA: Dept. of Civil and Environmental Engineering; 2008. 259p.

[5] Hallworth MA, Hogg AJ, Huppert HE. Effects of external flow on compositional and particle gravity currents. J Fluid Mech 1998;359:109–42.

[6] Hogg AJ, Hallworth MA, Huppert HE. On gravity currents driven by constant fluxes of saline and particle-laden fluid in the presence of a uniform flow. J Fluid Mech 2005;539:349–85.

[7] Villaret C, Lekien M, Claude B, Vinet V. Etude expérimentale de la dispersion des rejets par clapage d'un mélange de sable et de vase. He-42/97/072/a, LNHE, EDF; 1997.

[8] Villaret C, Claude B, Du Rivau JD. Etude expérimentale de la dispersion des rejets par clapage. He-42/98/065/a, LNHE, EDF; 1998.

[9] Boutin R. Dragage et rejets en mer. Les produits de type vase. Presses de l'ENPC; 2000. 307p.

[10] Morton BR, Taylor G, Turnner JS. Turbulent gravitational convection from maintained and instantaneous sources. Proc R Soc Lond 1956;A234:1–32.

[11] Krishnappan BG. Dispersion of granular material dumped in deep water. In: Scientific series, Environment Canada; 1975. p. 55. 113 p.

[12] Li CW. Convection of particle thermals. J Hydraul Res 1997;35(3):363–77.

[13] Garapon A, Villaret C, Boutin R. 3D numerical modelling of sediment disposal, Proceedings of the Physics of Estuarine. PECS; 2002. 13 p.

[14] Farout-Fréson I. Simulation numérique du clapage en mer: Etude du champ proche-Chute et Transport sur le fond. Thèse, Université Technologie de Compiègne; 2004. 316 p.

[15] Teisson C, Simonin O, Galland JC, Laurence D. Turbulence and mud sedimentation: a Reynolds stress model and a two-phase flow model. In: Proceedings of the 23rd ICCE, ASCE 1992; p. 2853–66.

[16] Villaret C, Davies AG. Modeling sediment-turbulent flow interactions. Appl Mech Rev 1995;48(9):601–9.

[17] Barbry N, Guillou S, Nguyen KD. Une approche diphasique pour le calcul du transport sédimentaire en milieux estuariens. CR Acad Sci (Série IIb) 2000;328:793–9.

[18] Chauchat J, Guillou S. On turbulence closures for two-phase sediment-laden flow models. J Geophys Res 2008;113:C11017. http://dx.doi.org/10.1029/2007JC00470.

[19] Nguyen KD, Guillou S, Chauchat J, Barbry N. A two-phase numerical model for suspended-sediment transport in estuaries. Adv Water Res 2009;32:1187–96. http://dx.doi.org/10.1016/j.advwatres.2009.04.00.

[20] Chauchat J, Guillou S, Barbry N, Nguyen KD. Simulation of the turbidity maximum in the Seine estuary with a two-phase flow model. CR Acad Sci Géosci (Série IIa) 2009. http://dx.doi.org/10.1016/j.crte.2009.04.00.

[21] Drew DA, Lahey RT. Analytical modelling of multiphase flow. In: Roco MC, editor. Particulate two-phase flow. Boston: Butterworth–Heinemann; 1993.

[22] Lundgren T. Slow flow through stationary random beds and suspensions of spheres. J Fluid Mech 1972;51:273–99. http://dx.doi.org/10.1017/S002211207200120.

[23] Graham AL. On the viscosity of suspensions of solid spheres. Appl Sci Res 1981;37:275–86. http://dx.doi.org/10.1007/BF0095125.

[24] Hsu T, Jenkins JT, Liu PLF. On two-phase sediment transport: dilute flow. J Geophys Res 2003;108(C3):3057. http://dx.doi.org/10.1029/2001JC00127.

[25] Peirano E, Leckner B. Fundamentals of turbulent gas–solid flows applied to circulating fluidized bed combustion. Prog Energy Combust Sci 1998; 24:259–96.

[26] Haider A, Levenspiel O. Drag coefficient and terminal velocity of spherical and non-spherical particles. Powder Technol 1989;58:63–70. http://dx.doi.org/10.1016/0032-5910(89)80008-7.

[27] Guillou S, Barbry N, Nguyen KD. Calcul numérique des ondes de surface par une méthode de projection et un maillage eulérien adaptatif. CR Acad Sci (Série IIb) 2000;328:875–81.

[28] Chorin AJ. Numerical solution of the Navier–Stokes equations. Math Comput 1968;22:745–62.

[29] Guillou S, Nguyen KD. An improved technique for solving two-dimensional shallow water problems. Int J Numer Methods Fluids 1999;29:465–83. doi:10.1002/(SICI)1097-0363(19990228)29:4<465::AID-FLD797>3.0.CO;2-H.

[30] Maxworthy T. Turbulent vortex rings. J Fluid Mech 1974;64(2):227–39.